NASA CR-172,298

NASA Contractor Report 172298

TRANSITION TO TURBULENCE IN PLANE CHANNEL FLOW

Sedat Biringen

OLD DOMINION UNIVERSITY RESEARCH FOUNDATION
Norfolk, Virginia 23508

NASA

National Aeronautics and
Space Administration

Langley Research Center
Hampton, Virginia 23665

TABLE OF CONTENTS

LIST OF FIGURES

N84-10577#

TABLE OF CONTENTS - concluded

LIST OF FIGURES - concluded

TRANSITION TO TURBULENCE IN PLANE CHANNEL FLOW

By

Sedat Biringen

SUMMARY

This work, performed under Grant No. NAG-1-228 from NASA/Langley Research Center, involves a numerical simulation of the final stages of transition to turbulence in plane channel flow. Three-dimensional, incompressible Navier-Stokes equations are numerically integrated to obtain the time-evolution of two- and three-dimensional finite-amplitude disturbances. Computations are performed on the CYBER-203 vector processor for a 32×51×32 grid. Results are presented for no-slip boundary conditions at the solid walls as well as for periodic suction-blowing to simulate active control of transition by mass transfer. Solutions indicate that the method is capable of simulating the complex character of vorticity dynamics during the various stages of transition and final breakdown. In particular, evidence points to the formation of a Λ-shape vortex and the subsequent system of horseshoe vortices inclined to the main flow direction as the main elements of transition. Calculations involving periodic suction-blowing indicate that interference with a wave of suitable phase and amplitude reduces the disturbance growth rates.

1. INTRODUCTION

Recent experiments by Nishioka, Asia & Iida (1981) have shown that transition to turbulence in a plane channel flow follows a sequence of events similar to that observed by Klebanoff, Tidstrom & Sargent (1962) in the boundary-layer transition. In this work, a direct numerical integration of the Navier-Stokes equations is performed in an attempt to simulate these events in plane channel flow, during the later stages of transition.

In their experiments, Nishioka et al. (1981) measured the streamwise mean and fluctuating velocities, U_1 and u_1', respectively, at a fixed streamwise location at a subcritical (linearly stable) Reynolds number, $Re = 5000$ and simulated the various stages of transition by varying the disturbance amplitude. Their observations show that subcritical instability takes place at a threshold amplitude of $(u_1')_{max}/U_0 = 0.01$, where U_0 is the mean velocity at the channel centerline. The evolution of this instability is evidenced by the intensification of the spanwise variation of the wavefront which develops into a peak-valley structure. Nishioka et al. (1981) observed that flow development follows a trend which is similar to transition in the boundary-layer (Klebanoff et al. 1962, Kovasznay, Komoda & Vasudeva 1962): local shear layers are formed away from the wall at spanwise peak positions ($u_1'/U_0 = 0.06$), these shear layers start to exhibit a "kink" which is the manifestation of secondary instability and is accompanied by a "spike" in the $u_1'/U_0 = 0.11$). In rapid succession, two-, three-, five-, and multi-spike stages are observed with increasing amplitude of the primary disturbance. Nishioka et al. (1981) presented evidence that in the final stages of transition, the flow starts to develop struc-

tures very similar to those found in fully developed wall turbulence. During this stage, the flow field is characterized by the development of a viscous sublayer, occurrence of the typical "streaks" close to the wall and the formation of horseshoe vortices sometimes referred to as the building blocks of wall turbulence (Theodorsen 1954). The present work simulates this sequence of events.

Effects of three dimensionality on transition have first been documented in detail by Klebanoff et al. (1962). Accordingly, three-dimensionality manifests itself mainly in the spanwise velocity variations resulting in the production of streamwise vorticity which, in turn, interacts with the spanwise vorticity and drives the flow to breakdown. Orszag & Kells (1980) and Patera & Orszag (1981) have expanded on this idea and studied the susceptibility of plane channel flow to three-dimensional disturbances by numerically integrating the three-dimensional Navier-Stokes equations. Their computations at subcritical Reynolds numbers revealed some interesting aspects of subcritical transition. They found that initially two-dimensional disturbances which are finite-amplitude two-dimensional Orr-Sommerfeld eigensolutions, decay slowly whereas the interaction of two-dimensional and three-dimensional disturbances drives the flow to instability for Reynolds numbers as low as 1000. In the present work we focus on the three-dimensional and nonlinear mechanisms that characterize transition in the final stages and during flow breakdown. Hence, we employ the full three-dimensional time-dependent Navier-Stokes equations. Calculations were performed at a linearly stable Reynolds number (Re = 1500), with finite-amplitude two- and three-dimensional eigensolutions of the Orr-Somerfeld equation used as the initial conditions. No attempt was made herein to study the effect of

different initial conditions or of Reynolds numbers; this is the subject of another investigation. We also investigated the idea of using periodic suction-blowing at the solid walls as a means of controlling transition. These computations were performed at Re = 7500 which is the linearly unstable range for this flow. Since transition control must be applied prior to the flow breakdown (e.g. before the occurrence of multi-spikes), disturbance amplitudes during these calculations were not large enough to impose stiff restrictions on the allowable time step.

In section 2, of this report, the numerical methods used in this study are briefly discussed. In section 3, results of calculations are presented and finally in section 4 a summary of results and some concluding remarks are given.

2. THE CALCULATION PROCEDURE

The calculation procedure is based on the incompressible Navier-Stokes equations in primitive-variable form,

$$\frac{\partial u_i}{\partial t} + u_\ell \frac{\partial u_i}{\partial x_\ell} = -\frac{1}{\rho} \frac{\partial p'}{\partial x_i} + \nu \frac{\partial^2 u_i}{\partial x_\ell \partial x_\ell} \tag{1}$$

and the continuity equation,

$$\frac{\partial u_i}{\partial x_i} = 0 \tag{2}$$

where u_i are the velocities along the x_i directions, ρ is the density, ν is the kinematic viscosity and p' is the total hydrostatic pressure. The equations are non-dimensionalized by the mean centerline velocity U_0 and the channel half-width, h. The flow is assumed to be driven by a constant mean pressure gradient $2/\text{Re}$, where Re is the Reynolds number given by $U_0 h/\nu$. Also, the convective terms are written in a form which prevents occurrence of nonlinear instability in the numerical solution procedure by ensuring conservation of momentum and energy (Mansour, Ferziger, & Reynolds 1978). The final form of the Navier-Stokes equations reads,

$$\frac{\partial u_i}{\partial x_i} + u_\ell \left(\frac{\partial u_i}{\partial x_\ell} - \frac{\partial u_\ell}{\partial x_i} \right) = -\frac{\partial P}{\partial x_i} + \frac{2}{\text{Re}} \delta_{i1} + \frac{1}{\text{Re}} \frac{\partial^2 u_i}{\partial x_\ell \partial x_\ell} \tag{3}$$

where $P = p'/\rho + \frac{1}{2} u_\ell u_\ell$ is the pressure head and $\delta_{i\ell}$ is the Kronecker delta.

The flow is assumed to be periodic in the streamwise x_1 and the spanwise x_3 directions along which the flow field variables can be expanded in terms of Fourier series. This enables the use of the pseudo-spectral method (Orszag 1972) to calculate the spatial derivatives along x_1 and x_3 by use of discrete Fourier transforms. Considering transforms in the x_1 direction, along which there are N_1 equally spaced mesh points, the velocity component u_1 can be written as

$$u_1(x_1) = \sum_{n_1 = -\frac{N}{2}}^{N/2-1} \hat{u}_1(k_1) e^{ik_1 x_1} \tag{4}$$

where $x_1 = m\Delta x_1$, $m = 0, 1, \ldots, N-1$ and $k_1 = 2\pi n_1 / N_1 \Delta x_1$. Accordingly, the Fourier transform of u_1 is

$$\hat{u}_1(k_1) = \frac{1}{N_1} \sum_{m=0}^{N_1-1} u_1(x_1) e^{-ik_1 x_1} \tag{5}$$

The spatial derivative of u_1 along x_1 can now be written as

$$\frac{\partial u_1(x_1)}{\partial x_1} = \sum_{n_1 = -N_1/2}^{N_1/2-1} ik_1 \hat{u}_1(k_1) e^{ik_1 x_1} \tag{6}$$

The derivative can be computed by forming the Fourier transform of $u_1(x_1)$, multiplying the result by ik_1 and computing the inverse transform. For

6

periodic functions, the pseudo-spectral method provides a means by which the spatial derivatives are evaluated with maximum accuracy for a given number of grid points. Along the x_2-direction, a mesh stretching that concentrates grid points close to the solid walls is employed (Moin, Reynolds & Firziger 1978). The resulting mesh enables the resolution of the sublayer that is formed during transition for y+ < 2, where y+ is the coordinate along x_2, in wall units. Spatial derivatives along x_2 are evaluated by a second-order finite-difference scheme on this non-uniform mesh.

The governing equations were numerically integrated by the semi-implicit method of Moin et al. (1978). This procedure employs the explicit Adams-Bashforth method for the convective terms and the implicit Crank-Nicholson method for pressure and for the viscous diffusion terms. In order to start the two time-level Adams-Bashforth method, the Euler-implicit method is used at the first time step.

Once the governing equations are discretized in time, a two-dimensional Fourier transform along the periodic directions x_1 and x_3 transforms the equations into the k_1-k_3 wave-number space. The transformed equations are written below in block-tridiagonal form for inversion along x_2

$$\underline{A}\,\underset{\sim}{F}_{j+1}^{n+1} + \underline{B}\,\underset{\sim}{F}_{j}^{n+1} + \underline{C}\,\underset{\sim}{F}_{j-1}^{n+1} = \underset{\sim}{R}_{j}^{n} \tag{7}$$

In (7), $\underline{A}$, $\underline{B}$, and $\underline{C}$ are coefficient matrices, $\underset{\sim}{F}_{j}^{n+1}$ is the solution vector at the advanced time level, n+1, and at the x_2-directional node, j; $\underset{\sim}{R}_{j}^{n}$ is right-hand side vector that contains the convective, diffusive and pressure terms at the previous time levels. These are given as

$$\underset{\sim}{F} = \begin{bmatrix} \hat{u}_1 \\ \hat{u}_2 \\ \hat{u}_3 \\ \hat{P} \end{bmatrix} \qquad \underline{A} = \begin{bmatrix} C2_j & 0 & 0 & 0 \\ 0 & C2_j & 0 & 0 \\ 0 & 0 & C1_j & 0 \\ 0 & 0 & C2_j & -Re.C1_j \end{bmatrix}'$$

$$\underline{B} = \begin{bmatrix} B2_j - \phi & 0 & 0 & \pm(k_1)_j Re \\ 0 & B2_j - \phi & 0 & \pm(k_3)_j Re \\ \mp(k_1)_j & \mp(k_3)_j & B1_j & 0 \\ 0 & 0 & B2_j - \phi & -Re.B1_j \end{bmatrix}$$

$$\underline{C} = \begin{bmatrix} A2_j & 0 & 0 & 0 \\ 0 & A2_j & 0 & 0 \\ 0 & 0 & A1_j & 0 \\ 0 & 0 & A2_j & -Re.A1_j \end{bmatrix}$$

and

$$R_1' = 0$$

$$R_2' = Re\left[-\frac{2u_1^n}{\Delta T} + \left(\frac{\partial^2 u_1}{\partial x_1^2} + \frac{\partial^2 u_1}{\partial x_3^2}\right)^n \right] + Re\,\frac{\partial P^n}{\partial x_1} - 2Re\left(\frac{3}{2}\,H_1^n - \frac{1}{2}\,H_1^{n-1}\right) - \frac{\partial^2 u_1^n}{\partial x_2^2}$$

$$R_3' = Re\left[-\frac{2u_2^n}{\Delta T} + \left(\frac{\partial^2 u_2}{\partial x_1} + \frac{\partial^2 u_2}{\partial x_3^2}\right)^n \right] + Re\,\frac{\partial P^n}{\partial x_2} - 2Re\left(\frac{3}{2}\,H_1^n - \frac{1}{2}\,H_2^{n-1}\right) - \frac{\partial^2 u_1^n}{\partial x_2^2}$$

$$R_4' = Re\left[-\frac{2u_3^n}{\Delta T} + \left(\frac{\partial^2 u_3}{\partial x_1^2} + \frac{\partial^2 u_3}{\partial x_3^2}\right)^n \right] + Re\,\frac{\partial P^n}{\partial x_3} - 2Re\left(\frac{3}{2}\,H_3^n - \frac{1}{2}\,H_3^{n-1}\right) - \frac{\partial^2 u_2^n}{\partial x_2^2}$$

8

also,

$$\phi \equiv \left[\frac{2Re}{\Delta T} + \left(k_1^2 + k_3^2\right)_j\right]$$

$$H_i = -u_\ell\left(\frac{\partial u_i}{\partial x_i} - \frac{\partial u_\ell}{\partial x_i}\right) \quad \text{(no summation over i)}$$

and,

$$R_j = \hat{R}_j'$$

Coefficients of the finite-difference operators that appear in the matrices $\underline{A}$, $\underline{B}$, and $\underline{C}$ are given as

$$C2_j = 2/\Delta_{j+1}(\Delta_{j+1} + \Delta_j), \quad B2_j = -2/\Delta_{j+1}\Delta_j, \quad A2_j = 2/\Delta_j(\Delta_{j+1} + \Delta_j)$$

$$C1_j = -A1_j = 1/(\Delta_{j+1} - \Delta_j)$$

$$\Delta_{j+1} = (x_2)_{j+1} - (x_2)_j$$

Since all the flow variables in the solution vector contain an imaginary and a real part, the block-inversion process is applied twice for each pair of k_1 and k_3, which are the wavenumbers along x_1 and x_3, respectively.

The assumption of periodicity in x_1 and x_3 eliminates the necessity of applying explicit boundary conditions along these directions. However, due to the presence of solid boundaries along the x_2 direction, no-slip

boundary conditions are imposed on u_1, u_2, and u_3 and the pressure at the wall is calculated by a second order approximation from the interior of the flow field. That the pressure boundary conditions are consistent with the x_2-momentum equation at the wall, has been shown by Moin et al. (1978).

Initial conditions were prescribed from the two- and three-dimensional eigensolutions of the Orr-Sommerfeld equation by considering that even for subcritical Reynolds numbers, plane channel flow can be driven to instability if the least stable two-dimensional finite-amplitude Orr-Sommerfeld eigenmodes are interacted with finite-amplitude three-dimensional eigenmodes (Orszag & Kells 1981). The most explosive situation arises when the three-dimensional eigenmodes are aligned with the main flow direction at ± 45 to ± 60 degrees. Accordingly, we have used the following initial condition:

$$\underline{u}(\underline{x}) = U(x_2,0,0) + u_{2D}(x_2)e^{i\alpha x_1} + u_{3D}(x_2)e^{i\alpha x_1 \pm i\beta x_3} \qquad (8)$$

Here, $U(x_2,0,0)$ is the parabolic velocity profile of plane channel flow. The eigenfunctions $u_{2D}(x_2)$ and $u_{3D}(x_2)$ correspond to two-dimensional and three-dimensional solutions of the Orr-Sommerfeld equation at Re = 1500, respectively. The two-dimensional solution was obtained for $\alpha = 1$ whereas, the three-dimensional solution was obtained for $\alpha = 1$, $\beta = \pm 1$. A computer program, which essentially uses the Kaplan filtering technique was used for the solution of the Orr-Sommerfeld equation (Reynolds 1967). The final amplitudes were chosen so that the maximum value of the x_1-directional two-dimensional disturbance was set equal to $0.11U_0$ and the maximum amplitudes of the x_1-directional three-dimensional disturbances were each set equal to $0.05U_0$.

3. RESULTS AND DISCUSSION

The finite-difference system (7) was solved on the CYBER-203 vector processor at NASA/Langley Research Center. A 32×51×32 mesh was employed along the x_1-, x_2-, and x_3-directions, respectively. The computer code was fully vectorized and vectorized library subroutines were used for the main computational operations that the solution technique employs. These vector operations are mainly one-dimensional fast Fourier transform (FFT) to calculate spatial derivatives with the pseudo-spectral method, two-dimensional FFT to transform the equations into k_1-k_3 wave-number space and block-tridiagonal matrix inversion along x_2. For the FFT operations, typical vector lengths were around 1000, which is an optimal vector length to take full advantage of the vector processor. For the block-tridagonal matrix inversion (which essentially is a scalar operation), a vectorized subroutine that inverts a large number of tridiagonal systems simultaneously was used. This procedure decreases CPU time significantly by reducing the number of scalar operations required to invert each system separately. The fully vectorized code takes about 10 sec. of CPU time per time step for the 32×51×32 mesh to solve the finite-difference system (7) on a computational box, in which the flow is confined between rigid walls at $x_2 = \pm 1$. Periodicity lengths (box lengths) along x_1 and x_3 were chosen so that the smallest wave numbers allowed in the computational domain were equal to $\alpha = 1$ and $\beta = 1$, respectively, i.e., the box length was set equal to 2π along these directions.

It should be recalled that the time-advancement scheme employed in this work is partly explicit (on the convective terms) and partly implicit (on the diffusion and pressure terms). Although in view of linear stability

analysis, implicit methods are unconditionally stable (extrapolation to nonlinear equations is sometime vague), the mixed nature of the present scheme as well as the time-accurate nature of the problem under investigation necessitate adherence to stability bounds of explicit schemes. Therefore, in all the calculations reported herein, the convective stability condition (the Courant-Friedrichs-Lewy condition) that requires the Courant number (C.N.) to be always less than one and the diffusive stability condition were obeyed. With $(\Delta x_2)_{min} = 0.0092$ and $\Delta T = 0.025$, where ΔT is the nondimensional time-step, through the course of the calculations C.N. varied as

$$C.N. \equiv \Delta T \left(\left| \frac{u_1}{\Delta x_1} \right| + \left| \frac{u_2}{\Delta x_2} \right| + \left| \frac{u_3}{\Delta x_3} \right| \right)_{max} < 0.2 \qquad (9)$$

whereas the diffusive stability criterion, D, varied as

$$D \equiv \frac{1}{Re} \left[\frac{\Delta T}{(\Delta x)^2_{min}} \right] < 0.04 \qquad (10)$$

so that the diffusive stability condition which requires D < 0.5, was also always satisfied. The computer program was tested by calculating the growth rates of small-amplitude Orr-Sommerfeld waves. For a wide range of Reynolds numbers (between 1000 and 10,000) the agreement between the computed results and the linear theory was better than 0.5%.

In the subsequent parts of this section, results obtained from the numerical integration of the finite-difference system (7) for the time-evolution of the initial disturbances are compared with the experiments of Nishioka et al. (1981). It should be noted that this experiment was done at Re = 5000 (subcritical) whereas the computation was done at a lower aubcritical Reynolds number, Re = 1500. The selection of a higher Reynolds

number (e.g., in the linearly unstable range) makes the governing equations very stiff and requires the use of extremely small time steps for numerical stability. Hence, the selection of Re = 1500 was mainly to force the computations into transition and breakdown with the least amount of computer expense. It should be noted that wall phenomena characteristic of the final stages of transition are essentially independent of Reynolds number as observed by Nishioka et al. (1981) for channel flow and by Smith & Metzler (1982) for boundary-layer transition. Therefore, the difference between the Reynolds numbers of the experiment and the simulation should not have any important consequences for the qualitative comparisons between the two sets of results.

3a. Plane Channel Flow with No Mass Transfer

In their experiments, Nishioka et al. (1981) identified the various stages of transition according to the number of spikes appearing in the oscilloscope traces of the disturbance velocity, u_1'. Since the time-axis of the experiment is interchangeable with the x_1-axis of the computation, we obtain similar traces by plotting u_1' along x_1 (over two periods) as shown in figure 1. In this figure, the first frame shows the sinusoidal variation of the initial conditions at T = 0. This is followed by the nonlineaer distortions of the initial conditions resulting in variations of u_1' which strongly resemble the oscilloscope traces at the one-, three-, and five-spike stages of the laboratory flow. In particular, the variations of u_1' with x_1 at T = 44 are very similar to the ensemble-averaged waveforms presented by Nishioka et al. (1981) at the five-spike stage. The last frame in figure 1 shows variations of u_1' at a time (T = 79) much later than the occurrence of the five-spike stage (T = 44). Hence, we note the absence of

fluctations of rich frequency content that are characteristic of fully-developed turbulence; this lends support to the idea that the last stage of transition may not be spontaneous and explosive a phenomenon as generally supposed. However, at this stage, the u_1' variations are very similar to velocity oscillations observed in wave packets and indicate the occurrence of "patches" of turbulent fluid. For the remainder of this discussion, results from the simulation at the spike stages (shown in figure 1) will be used, whenever possible, for comparisons with the corresponding spike stages of the experiments of Nishioka et al. (1981).

In figure 2, we show a history of the time-evolution of the flow in terms of the maximum amplitude of the two dimensional primary disturbance, its two-dimensional harmonic and the three-dimensional primary disturbance. The trends displayed by these quantities are generally similar to the results of Orszag & Kells (1980) which they obtained from computations performed at Re = 1250. The main features of these trends are the rapid decrease in the two-dimensional primary-wave amplitude and the rapid increase of the amplitude of its harmonic. Also, the three-dimensional primary-wave amplitude first increases, then gradually decreases at around T = 30. In the present calculations, we observe that variations of the amplitudes start to fluctuate as early as T = 15 but, even at later times, the fluctuations do not display an explosive trend. That no "explosive" instabilities were found in the present computations is in accord with the findings of Nishioka, Asai & Iida (1980), which imply that breakdown in channel flow is as gradual as the growth of instabilities found in free shear flows.

In figure 3, we present plots of maximum root-mean-square (rms) ampli-

tudes of u_1, $(u_1\;_{rms})_{max}$, over two periods along x_3. Here, we define the rms value as an average over x_1. We note that at $T = 0$, the wave pattern is sinusoidal and corresponds to peaks at $x_3 = 0$, 2π, 4π and to valleys at $x_3 = \pi$, 3π. Subsequently, at later times the nonlinear distortions of the wave front result in minima occurring at the peaks and maxima occurring at the valleys in accordance with the experiments of Nishioka et al. (1980). At later times, an increase in the frequency of the peak-valley structures is clearly evident suggesting an increase in the number of characteristic vortex structures along x_3.

Plots of velocity profiles averaged over the x_1-x_3 plane, $\langle u_1 \rangle$, are shown in figure 4 for laminar (initial), late transition and "early turbulence" stages at $T = 0$, $T = 44$ and $T = 79$, respectively. The $\langle u_1 \rangle$ distribution at $T = 79$ has a strong resemblance to the turbulent channel flow profile, with increased velocity gradient at the wall and with a full profile indicative of turbulent mixing. Although, as expected, $\langle u_1 \rangle$ profiles do not show any fluctuations (or inflections), plots of instantaneous velocity profiles do show very strong inflections, especially in the regions close to the walls (figure 5). This indicates that the interaction of two- and three-dimensional waves close to the walls is the central mechanism that drives the flow to instability. This is in accord with the idea that the flow will undergo transition only for a selected band of spanwise wave numbers, the most "dangerous" of which result in three-dimensional disturbances with maxima occurring close to the walls (Orszag & Kells 1980). In figure 6, the velocity profile $\langle u+ \rangle = \langle u_1 \rangle / u_\tau$ versus $y+ = x_2\, u_\tau/\nu$ is plotted; here u_τ is the friction velocity and is calculated from $d\langle u_1 \rangle/dx_2$

at the wall times $1/Re$. Although, the plots indicate the formation of a sublayer, and the change from $T = 44$ to $T = 79$ shows a gradual approach to the law-of-the-wall, the difference is still especially apparent in the logarithmic region. At $T = 44$, the Reynolds number based on friction velocity is equal to 69 and, as expected, is larger than its initial (laminar) value of 55.

Plots of plane-averaged fluctuations intensities, $\langle(u_1 - \langle u_1\rangle)^2\rangle$, are shown in figure 7 at various T. There are several interesting features of this figure. Firstly, at $T = 17$, the shift in the position of peak amplitude towards the channel center $(x_2 = -0.6)$, as well as the increase in the maximum amplitude indicate that the development of the computed flow field is compatible with experimental observations pertaining to the one-spike stage of the transition process (Tani 1969). It will later be shown that during this stage there is a substantial increase in the spanwise vorticity, ω_z, away from the lower wall around $x_2 = -0.6$. Secondly, in accordance with the laboratory flow of Nishioka et al. (1981) at later stages, the computed intensity profile displays a second peak occurring close to the wall associated with turbulence production. At $T = 44$ corresponding to the five-spike stage, we see that peak intensity has reached a value typical of turbulent channel flow; however, the peak occurs uncharacteristically away from the wall. Finally at $T = 79$, the peak in the intensity profile has moved towards the wall but even at this stage, the distribution has not assumed the asymptotic fully-turbulent form. In figure 8, plots of plane-averaged shear stress, $\langle u_1 - \langle u_1\rangle)u_2\rangle$, profiles are shown. The increase in the magnitude of shear stress from $T = 0$ to $T = 17$ clearly indicates the effects of nonlinearity in transferring energy from the mean

flow to the fluctuating motion. At the five-spike stage (T = 44), the maximum shear stress has attained a value typical of turbulent channel flow. However, the locatiion of the maximum is away from the wall and roughly corresponds to the location of the peak in the respective intensity profile (figure 7). It can thus be inferred that at this stage of the comutation, the energy-exchange mechanisms of fully-developed wall turbulence is not yet reflected by the plane-averaged velocity correlations.

Spanwise variations of u_1 are plotted at various distances along x_2 in figures 9a-9e. In figure 9a, we show initial distributions which are highly three-dimensional. At T = 17 (figure 9b), the distributions indicate a velocity defect both at peak and valley as well as a velocity excess in between. This is indicative of intensification of the initial streamwise vortices and appearance of weaker streamwise vortex pairs in accordance with the Benney-Lin (1960) theory. Subsequently, figures 9c-9e display the formation of additional vortex pairs indicating transport of energy down the wave-number spectrum. The spanwise symmetry imposed by the initial conditions is retained through the five-spike stage. At this stage, an estimate of the flow field resolution can be obtained from the spanwise distance between peak positions, λ_z. Nondimensionalised by u_2 and ν, typically λ_z = 115. This is larger than but comparable to λ = 80, which is the typical spanwise length in the laboratory flow during the five-spike stage (Nishioka et al. 1981). It should be noted that the spanwise characteristic length in wall turbulence is about 100. Therefore, it could be asserted that at this stage present results are representative of <u>initial</u> wall turbulence.

A more detailed description of the transition process can be obtained from contour plots of equi-shear lines, $\partial u_1 / \partial x_2$ (which correspond to

approximate spanwise vorticity, ω_z) in the $x_1 - x_2$ plane at the position of maximum u_1/U_0. Results from the computation that correspond to the various stages of the laboratory flow are presented in figures 10-15 between the lower wall $(x_2 = -1.0)$ and channel center $(x_2 = 0.0)$. In figures 11a - 13a, figures 4-6 of Nishioka et al. (1981) are also shown for a qualitative comparison with the present results. In figure 10, contour plots corresponding to the initial conditions and in figure 11, contour plots corresponding to the "one spike" stage $(T = 0$ and $T = 17$, respectively) are shown. In both the laboratory flow and the computation, the typical head of the shear layer appears very clearly at the one-spike stage, indicating the formation of a shear layer away from the wall at about $x_2 = - 0.6$ due to the induced velocity from the streamwise vortex system. In addition, the sudden dip of the shear layer from the high-velocity outer flow to the low-velocity region clearly appears as a kink in both the computation and the laboratory flow. Since the grid points are finely clustered along x_2 close to the wall, vorticity concentrations in this region are also adequately resolved by the numerical simulation.

Figure 12 shows equi-shear lines at $T = 27$ corresponding to the three-spike stage of the laboratory flow. Due to the secondary instability manifested in the previous stage, breakdown of flow structures into smaller scales is observed in both the experiment and the computation. The growth of the kinked portions of the equi-shear lines into the so-called "hairpin eddies" is clearly depicted in the experiment. The computation displays a similar evolution: the head of the shear layer is lifted up towards the channel centerline, and the kink in the shear layer is quite apparent in this stage of the simulation. Simultaneously with this activity taking

place in the outer (high speed) portions of the flow field, both the experiment and the computation show an intense shear layer developing close to the wall, which is indicative of turbulence generation. It is generally agreed that hairpin eddies which are lifted towards the centerline erupt into turbulent spots. However, figure 12 indicates that wall turbulence may also be closely associated with vorticity dynamics simultaneously taking place with the eruption of hairpin eddies. Contours of equi-shear lines at T = 44 corresponding to the five-spike stage of the experiment are shown in figure 13. In both the experiment and the computation, the intense shear layer developed in the wall region is closely discernible. It should also be noted that, the spanwise position of maximum ω_z which appears very close to the wall and does not necessarily coincide with the spanwise location of maximum u_1/U_0 where the contours are presented. The most significant feature of figure 13 is the existence of distinct vortex structures in the wall region both in the laboratory flow and in the computation. These vortices are inclined to the main flow direction at an angle that varies between approximately 14° to 40° and show a close resemblance to the energetic horseshoe vortices characteristic of initial wall turbulence (Hama & Nutant 1963, Klebanoff et al. 1962). It is these vortices roughly aligned along the direction of maximum extensional stress that are mainly responsible for extracting energy from the mean shear (Tennekes & Lumley 1972).

In figure 14, equi-shear lines at spanwise locations $x_3 = (x_3)_0 + 2\Delta x_3$ and $x_3 = (x_3)_0 + 4\Delta x_3$ at T = 44 are compared. Here, we define $(x_3)_0$ as the spanwise position corresponding to figure 13 and Δx_3 is the mesh size along x_3. Figure 14 suggests that the shear layer is formed from a system of horseshoe vortices in succession such that as the first-born vortex

erupts into the channel center, a new one forms at the wall. As evidenced in Figure 5, the vortex lift-up is still clearly discernible at the "early turbulence" stage (T = 79). Here, we note the vortex lift-up towards the channel center but its extension is considerably shorter than that observed previously at the five-spike stage. This variance suggests the existence of different vortex structures characteristic of these two stages. In fact, we shall later show that the typical horseshoe vortex of late transition is not the basic structure of early turbulence.

As we have noted before, the mechanism that is responsible for the generation of vorticity concentrations is usually explained as vortex stretching (and deformation) by the mean flow. The stretching and deformed layer moves downstream with a translation velocity that induces lower local velocity of the upstream edge of the vorticity layer than its downstream edge (Komoda 1967). An examination of u_1 contours of (figures 16 and 17) along with the approximate spanwise vorticity contours at T = 27 (figure 12b) and at T = 44 (figure 13b) in the $x_1 - x_2$ plane clearly shows a similar trend. We observe that the nose of the vorticity layer is generally associated with higher velocities than the upstream region and large variations of the local velocity exist within the layer.

Finally, normal velocity, u_2, contours are shown in figures 18-21 during the three-spike, multi-spike and early-turbulence stages at the position of maximum u_1/U_0. Figure 26 shows u_2-contours in the $x_1 - x_2$ plane at T = 27, corresponding to the three-spike stage of the laboratory flow. In this figure, there is clear evidence of the beginning of an alternating up-and-down flow similar to the pattern described by Kovaszny et al. (1967), which is characterized by the intense updrift accompanied by fluid

drifting down at both sides. This alternating structure of up-and-down flow in the x_1 - x_2 plane is more evident at T = 44 (figure 19), corresponding to the multi-spike stage of the experiment. Also in this figure, alternating regions of fluid with scales smaller than those at T = 27 are depicted. In figure 20 and 21, normal velocity contours are shown in the x_2 - x_3 plane at T = 44 and T = 79 corresponding to the multi-spike and early-turbulence stages, respectively. These contours are plotted in the region between the lower wall (x_2 = -1.0) and x_2 = -0.92, display the evolution of alternating structures very similar to the characteristic streak-like structures found in the wall region of turbulent channel flow (Moin & Kin 1982).

3b. Active Control of Transition by Periodic Suction-Blowing

In this section we demonstrate the usefulness of employing periodic suction-blowing boundary conditions at the solid walls for controlling transition. All these calculations were performed at a Reynolds number well within the linearly unstable range, i.e. at Re = 7500. The main idea here is to cancel or modify the "most dangerous" disturbance by interfering with a wave of suitable amplitude and phase. This idea has been proven to be effective in controlling boundary-layer transition in an experiment in which the two-dimensional Tollmien-Schlichting wave was effectively cancelled by a control wave generated downstream of the initial disturbance. The amplitude and phase of the control wave (produced by a second wave generator placed downstream of the first) was adjusted to minimize the maximum disturbance from the first wave generator (Milling 1981). Expanding on this idea and assuming the two-dimensional primary wave to be the most dangerous disturbance, in this work we prescribe the boundary conditions at the solid walls such that

(a) the resulting control wave is compatible with flow periodicity along x_1 and x_3 so that there will be no net mass transfer into the flow field;

(b) the resulting control wave will be 180° out of phase with the two-dimensional primary wave;

(c) the control wave amplitude is adjusted for maximum attenuation of the primary disturbance.

In figure 22, results for a case in which the initial disturbances are two-dimensional solutions of the Orr-Sommerfeld equation are shown. The maximum amplitude of u_1' was set equal to 1% of the channel centerline velocity. Periodic suction-blowing boundary conditions were prescribed at each wall at $T = 5.3$ for one time stop, before and after which the channel walls were made impermeable via the no-slip boundary conditions. The most effective wave produced by the suction-blowing boundary conditions was found to be 180° out of phase with the two-dimensional primary u_2' (corresponding to $\hat{u}_2(1,0)$ in the Fourier space) with twice its amplitude. The effect of the control wave to reduce the growth rates of both $(u_1')_{2D}$-primary and its harmonic is evident from figure 22. In fact, the control wave has resulted in a <u>decaying</u> harmonic preventing energy transfer down the wave-number spectrum, consequently inhibiting the proper development of the transition process.

To test the effects of three-dimensionality a similar calculation was performed in which three-dimensional solutions of the Orr-Sommerfeld equation were also included into the initial disturbance field. For this case, the maximum amplitudes of the two- and three-dimensional disturbances were

set at 3% and 1% of the channel centerline velocity, respectively. The most effective control wave was found to be 180° out of phase with $(u_2')_{2D}$ with 2.5 times its amplitude. The characteristics of the resulting flow field are shown in figure 23, after the periodic suction-blowing boundary conditions are applied at $T = 5.3$ for one time step. In summary, the control wave attenuated the growth rates of $(u_1')_{total}$ and $(u_1')_{2D}$ - primary, and resulted in a decaying $(u_1')_{2D}$ - harmonic as in the previous case. Note that $(u_1')_{3D}$ - primary remained unchanged.

It is apparent from the preceding discussion that the application of periodic suction-blowing boundary conditions on the solid walls of the channel has a considerable effect in reducing the growth rates of two- and three-dimensional disturbance fields. In practice the technique can be implemented via a suction-blowing strip along the body span. The spectrum of the disturbance field just upstream of the strip must be available in order to activate the correct boundary conditions and obtain the most effective control wave. Further work is necessary to evaluate the frequency-response and feedback delay of such a mechanism.

4. SUMMARY AND CONCLUDING REMARKS

In this study, final stages of transition to turbulence in plane channel flow have been simulated by a direct numerical solution of the Navier-Stokes equations. It is found that, in spite of the limited resolution of the 32x51x32 grid employed in the computations, the simulation is capable of reproducing most of the essential features of wall phenomena observed in the laboratory. Grid resolution in the x_1 and x_3 directions, along which the flow is periodic, is found to be adequate to capture the sequence of events that lead to early turbulence. Vorticity contours in the vicinity of the lower wall indicate formation of a system of horseshoe vortices with legs or extensions in the $x_1 - x_3$ plane comprised of counter-rotating streamwise vortex pairs. Our findings are also in accord with the Benney-Lin (1960) theory, e.g., the present computations clearly depict frequency-doubling of streamwise vorticity. It should be noted that the initial conditions used in this work are of the Benney-Lin type and consist of a vorticity field with a strong spanwise component and weak streamwise and transverse components. Therefore, the question of the origin of stream-wise vorticity and its precise relation to distortions of spanwise vorticity remain to be addressed in future work.

At later stages of the computation, transverse velocity contours indicate the formation of streak-like structures alternating in the spanwise direction. Typically, the spanwise characteristic length of these vortices, inferred from the spanwise variations of u_1, was found to be approxiamtely $\lambda_z = 115$; this is close to $\lambda_z = 100$ of fully-developed wall turbulence. It was found that during the later stages of transition, flow field statistics indicate the formation of a laminar sublayer; however, the

development of the logarithmic region and consequently the approach to fully-developed turbulence is slow. This gradual approach to steady state is also reflected in the profiles of plane-averaged intensity and shear stress.

The main deficiency of this study stems inevitably from limited spatial resolution and manifests itself in several ways. Firstly, at later stages of the computation, insufficient mesh resolution results in lower gradients of the mean velocity in the viscous sublayer. This, in turn, causes less turbulence production in the wall region as evidenced by the absence of peaks in the intensity and shear-stress profiles close to the wall. Secondly, the finite cut-off wave numbers along x_1 and x_3 preevent the formation of a proper wave-number spectrum. As a consequence, pollution of Fourier modes and accumulation of excess energy at low wave numbers become very significant sources of accuracy at large T. Hence, proper simulation of transition beyond the early-turbulence stage necessitates the use of higher grid resolution. Even then, the incorporation of a mechanism to account for the subgrid scale turbulence would be required for a more accurate and realistic representation of the flow field phenomena.

REFERENCES

Benney, D. J. of Lin, C.C. 1960 On the secondary motion induced by oscillations in a shear flow. Phys. Fluids 4, 656.

Hama, F.R. & Nutant, J. 1963 Detailed flow field observations in the transition process in a thick boundary layer. Proc. 1963 Heat Transfer and Fluid Mech. Institute, Stanford Univ. Press.

Klebanoff, P.S., Tidstrom, K.D. & Sargent, L.M. 1962 The three-dimensional nature of boundary-layer instability. J. Fluid Mech. 12, 1.

Komoda, H. 1967 Nonlinear development of disturbance in a laminar boundary layer. Phys. Fluids. 10, Suppl., 87.

Mansour, N.N., Ferziger, J.H. & Reynolds, W.C. 1978 Large eddy simulation of a turbulent mixing layer. Dept. Mech. Engng. Stanford Univ. Rep.TF-11.

Milling, R.W. 1981 Tollmien-Schlichting wave cancellation. Phys. Fluids.

Moin, P. & Kim, J. 1982 Numerical investigation of turbulent channel flow. J. Fluid Mech. 118, 341.

Moin, P., Reynolds, W.C. & Ferziger, J.H. 1978 Large eddy simulation of incompressible turbulent channel flow. Dept. Mech. Engng. Stanford Univ. Rep. TF-12.

Nishioka, M., Asai, M. & Iida, S. 1980 An experimental investigation of the secondary instability. In Laminar-Turbulent Transition (ed.R. Eppler of H. Fasel), Academic Press, 37.

Nishioka, M., Asai, M. & Iida, S. 1981 Wall phenomena in the final stage of transition to Turbulence. In Transition and Turbulence (ed. R.E. Meyer), Academic Press, 113.

Orszag, S.A. 1972 Comparison of pseudo spectral and spectral approximation. Studies in Appl. Math., LI, No. 3, 253.

Orszag, S.A. & Kells, L.C. 1980 Transition to turbulence in plane Poiseuille and plane Couette flow. J. Fluid Mech., 96, 159.

Orszag, S.A. & Patera, A.T. 1981 Subcritical transition to turbulence in planar shear flows. Phy. Rev. Let. 45, 989.

Reynolds, W.C. 1967 A Fortran IV program for solution of the Orr-Sommerfeld equation. Dept. Mech. Engng. Stanford Univ. Rep. FM-4.

Smith, C. R. & Metzler, S. P. 1983 The characteristics of low-speed streaks in the near-wall region of a turbulent boundary layer. J. Fluid Mech., 129, 27.

Tani, I. 1969 Boundary layer transition. <u>Ann</u>. <u>Rev</u>. <u>Fluid</u> <u>Mech</u>. <u>1</u>, 169.

Tennekes, H. & Lumley, J.L. 1972 <u>A First Course in Turbulence</u>. MIT Press.

Theodorsen, T. 1955 The structure of turbulence in <u>50 Jahre Grenzschichtfo-</u>
<u>rschung</u>. Friedr. Vieweg of Sohn, 55.
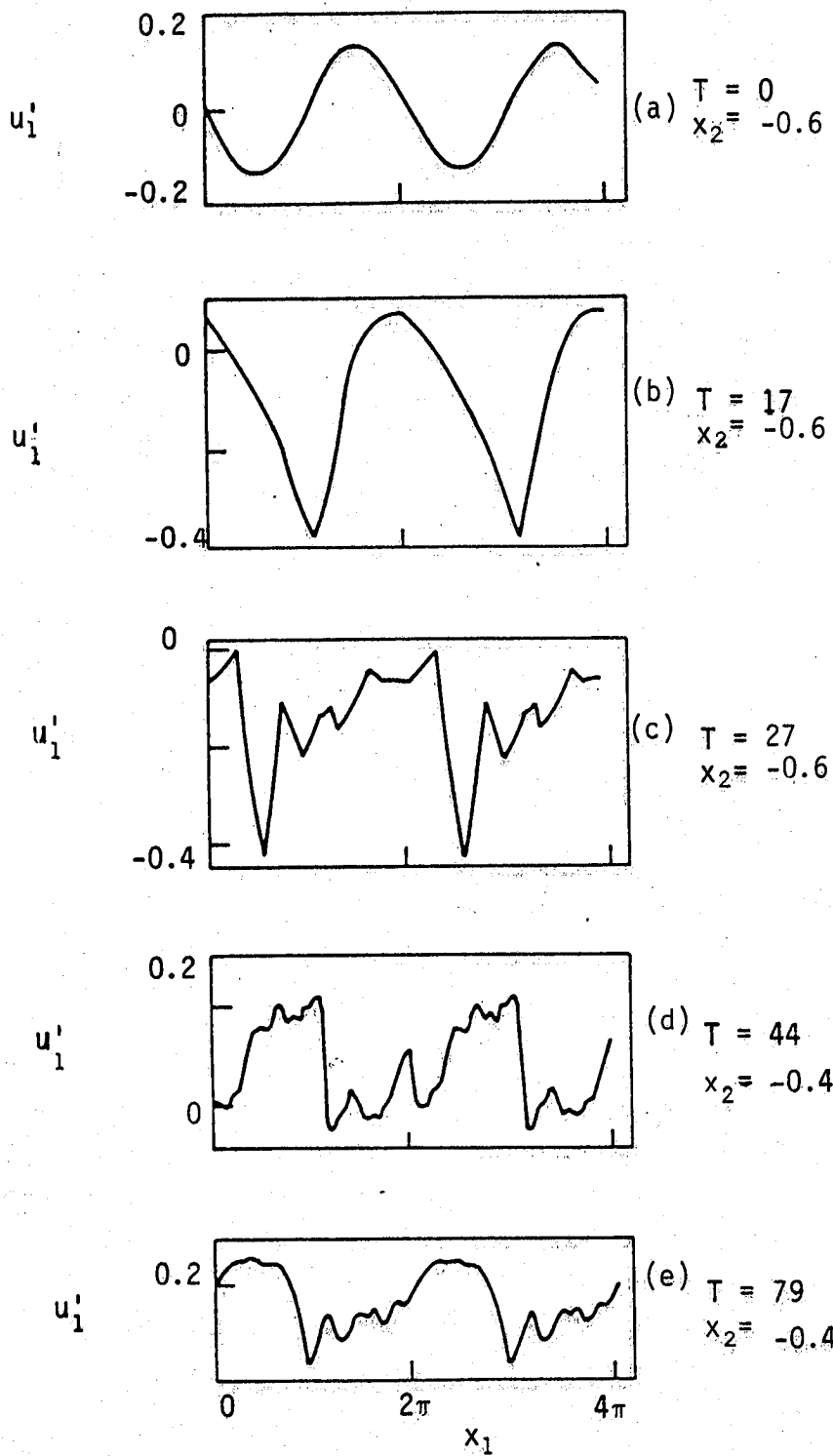
Figure 1. Development of u_1' fluctuation in time along x_1.
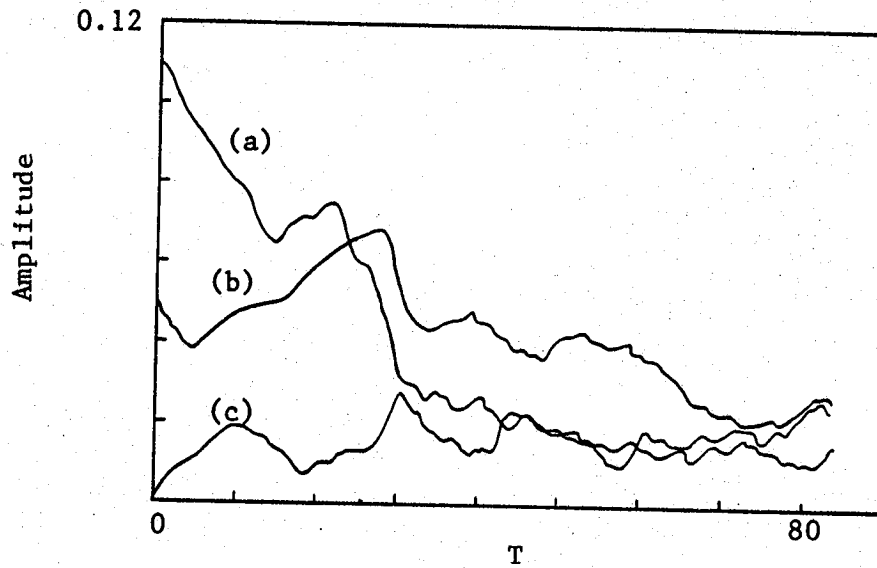
Figure 2. Time-history of maximum disturbance amplitudes.
(a) Two-dimensional primary; (b) three-dimensional
primary; (c) two-dimensional harmonic.
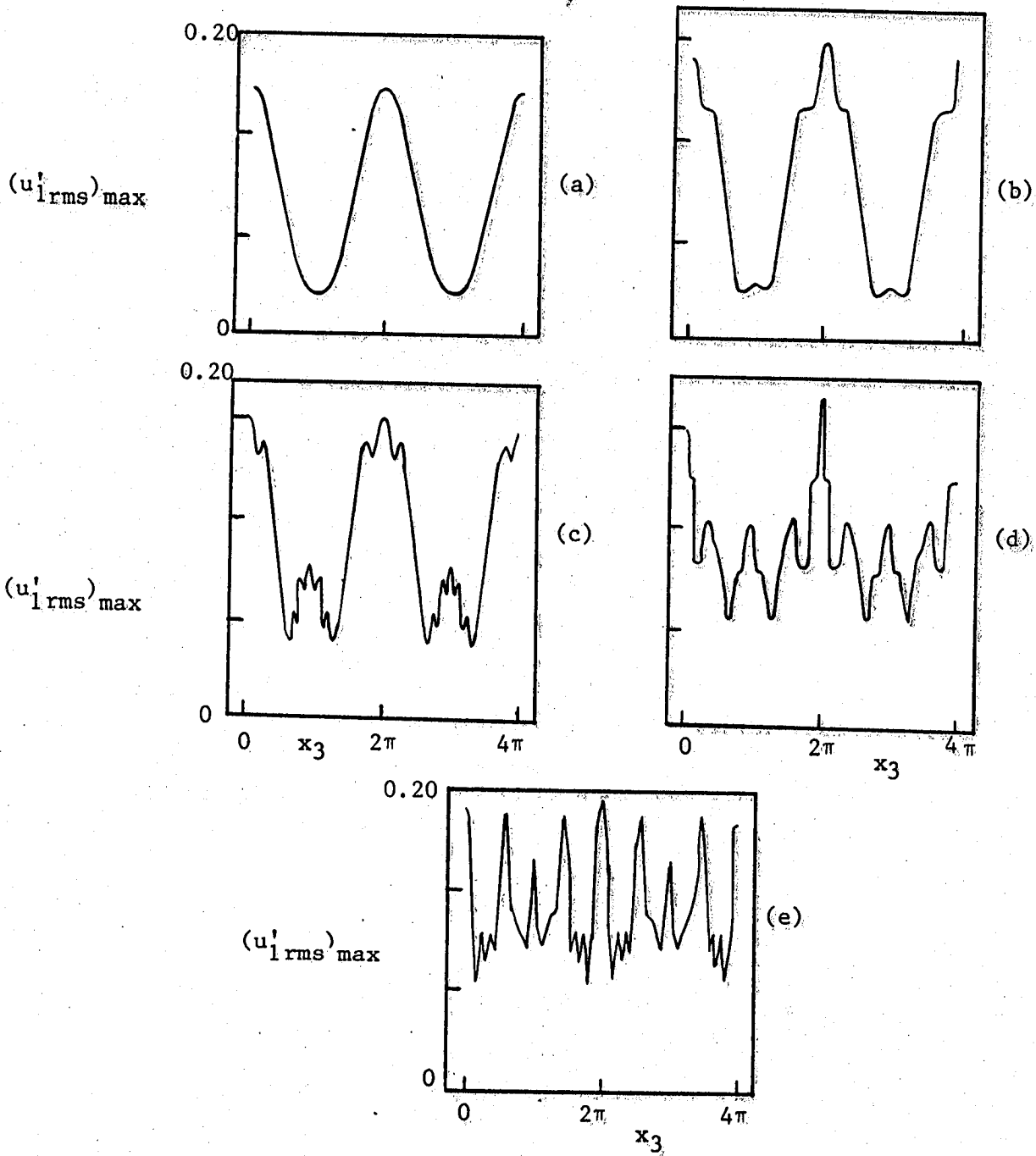
Figure 3.   Development of the peak-valley structure in terms of
            maximum $(u_1')_{rms}$.   (a) T=0; (b) T=17; (c) T=27; (d) T=44;
            (e) T=79.
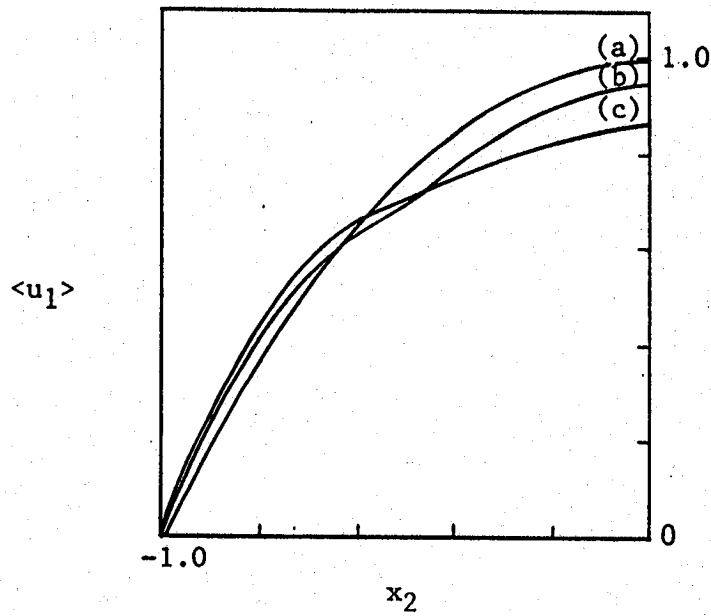
Figure 4. Plots of plane-averaged mean velocity profiles.
(a) T=0; (b) T=44; (c) T= 79.
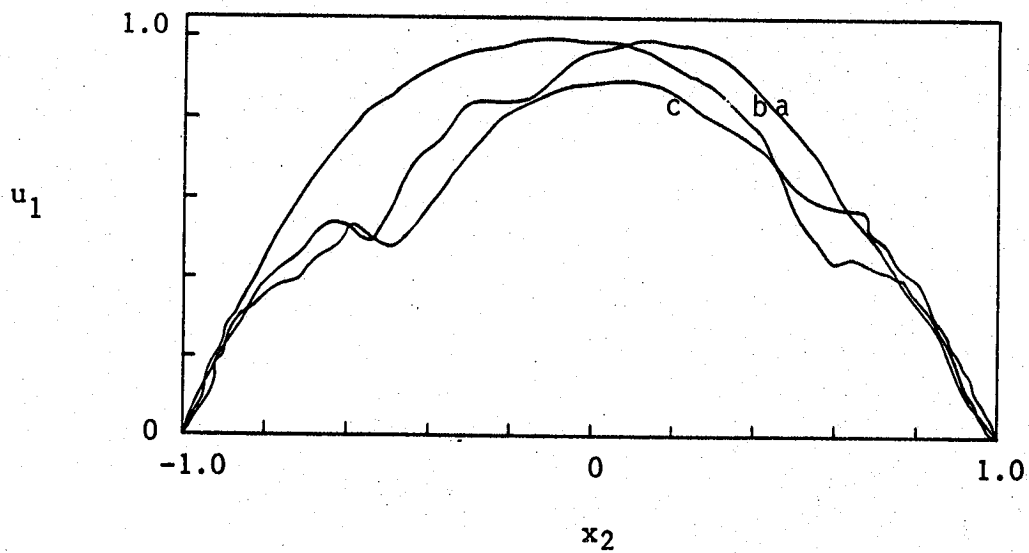
Figure 5. Plots of instantaneous velocity profiles at x_1= $3\pi/2$,
x_3= $\pi/2$. (a) T=17; (b) T=44; (c) T= 79.
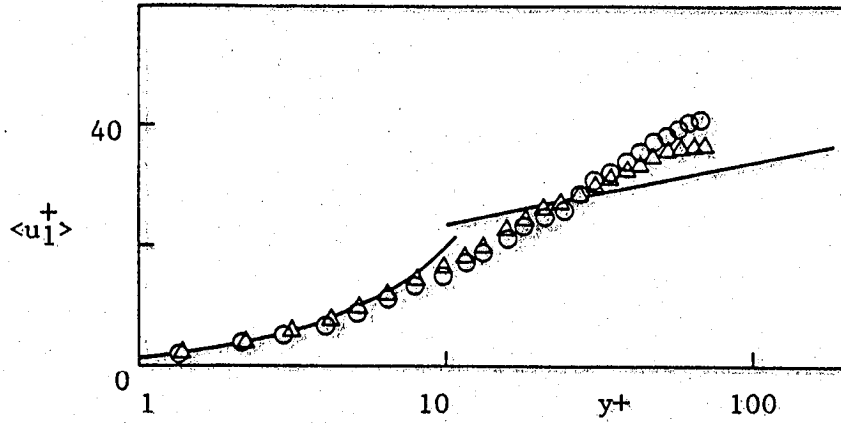
Figure 6. Plots of plane-averaged mean velocity in wall units. O, T = 44; Δ, T = 79.
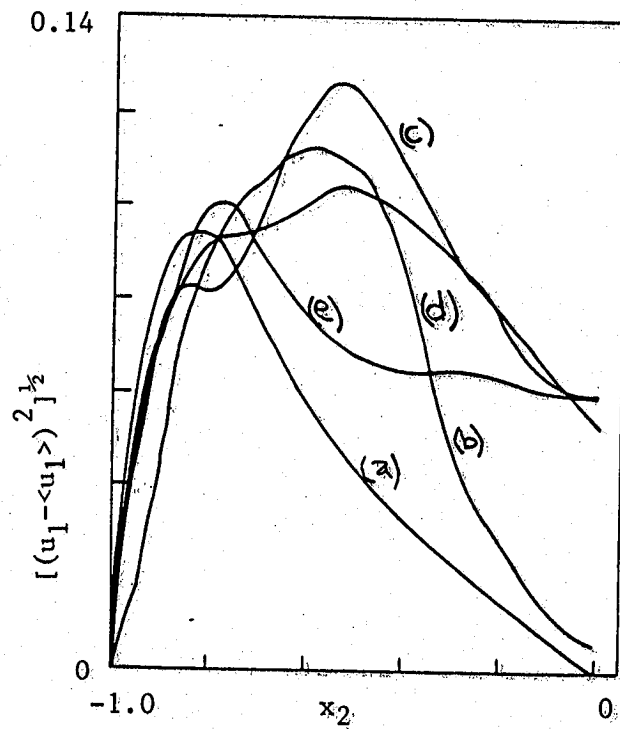
Figure 7. Plots of plane-averaged fluctuation intensities of u_1. (a) T = 0; (b) T = 17; (c) T = 27; (d) T = 44; (e) T = 79.
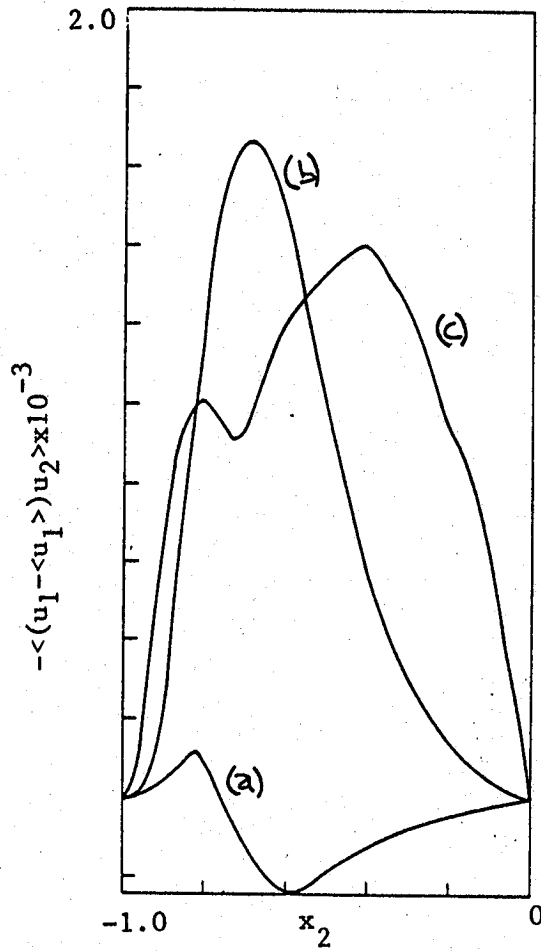
Figure 8. Plots of plane-averaged shear stress. (a) T = 0; (b) T = 17; (c) T = 44.

33
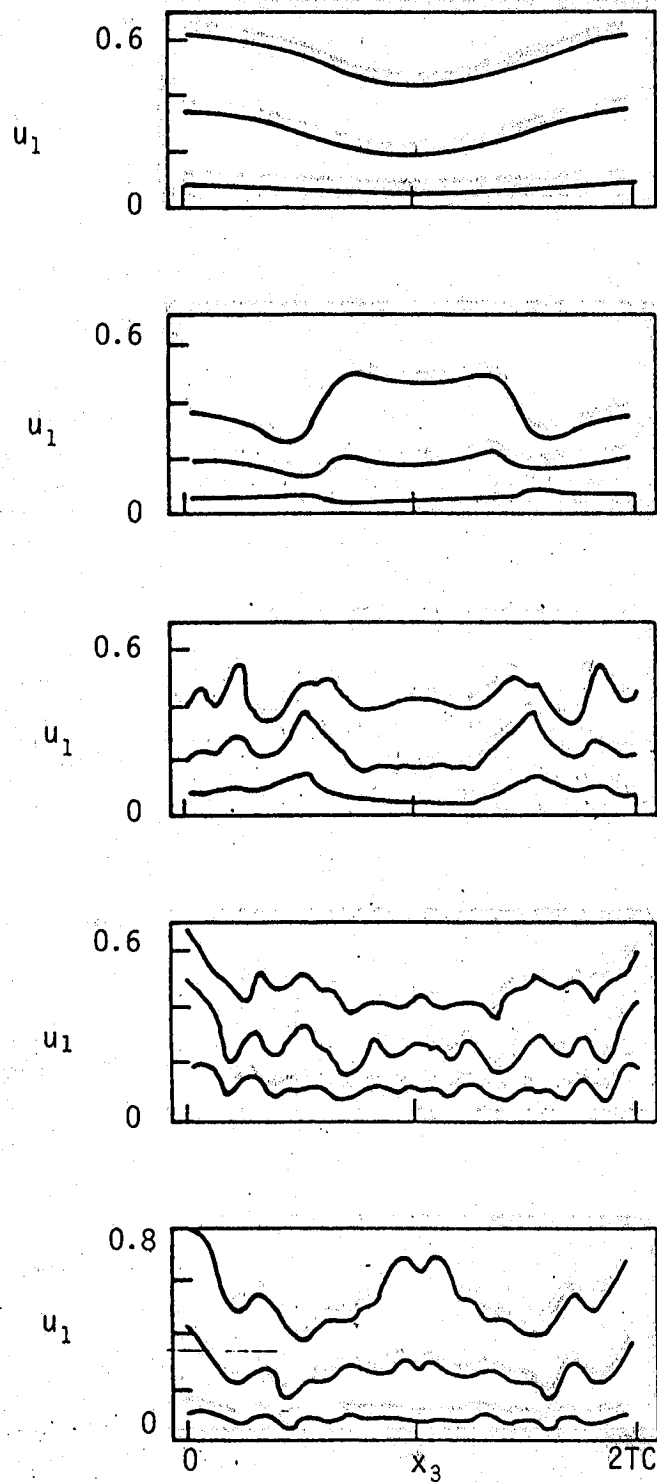
Figure 9. Spanwise variations of u_1. (a) $T = 0$; (b) $T = 17$; (c) $T = 27$;
(d) $T = 44$; (e) $T = 79$. (i) bottom, $x_2 = -0.968$; (ii) middle, $x_2 = -0.903$;
(iii) top, $x_3 = -0.764$.
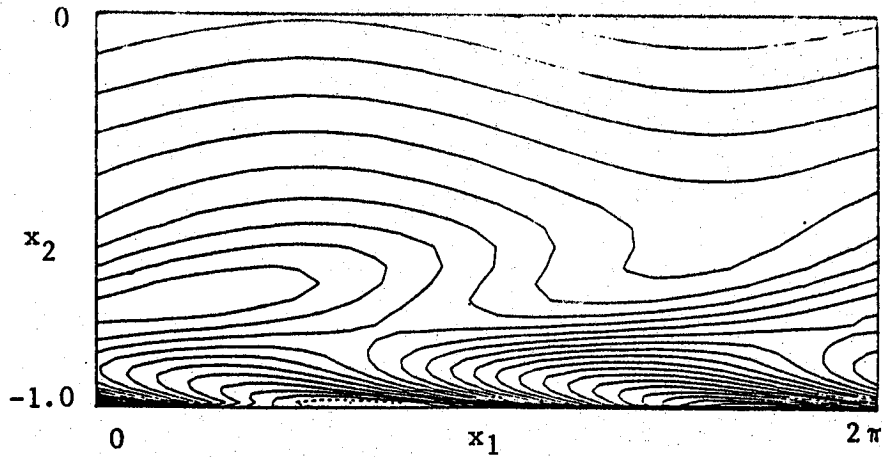
Figure 10.   Contour plots of $\partial u_1 / \partial x_2$ at $T = 0$ in the x_1-x_2 plane; contours from -4.0 to 4.2.

(a)

(b)
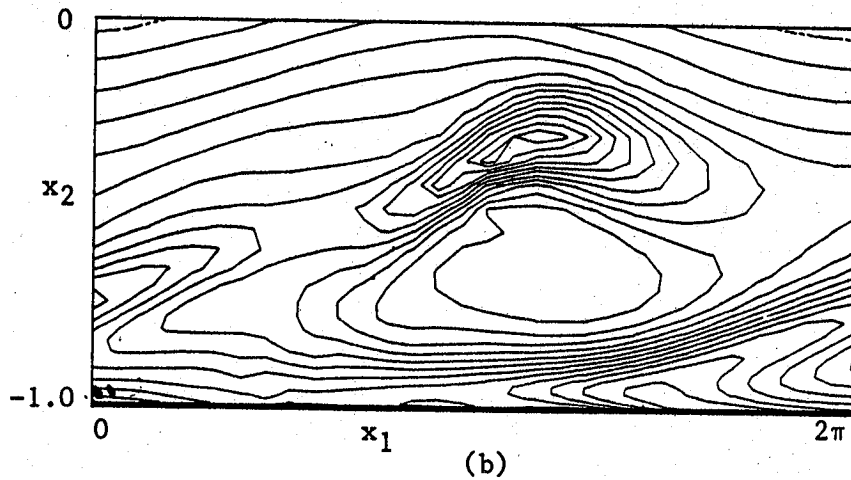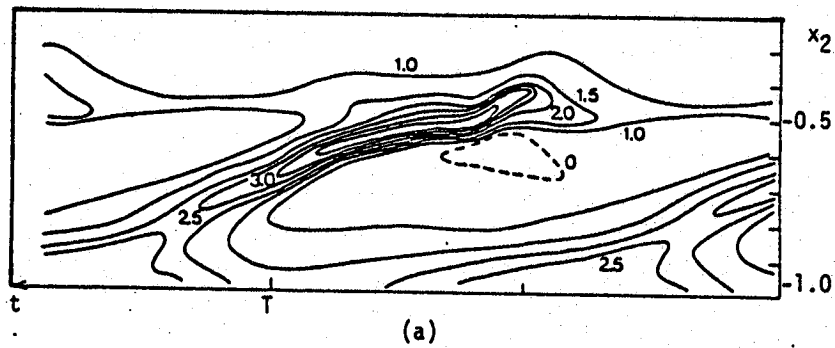
Figure 11.   Contour plots of $\partial u_1 / \partial x_2$.   (a) One-spike stage, figure 4 from Nishioka et al. (1981); (b) computations at $T = 17$ in the x_1-x_2 plane, contours from -0.2 to 2.6.
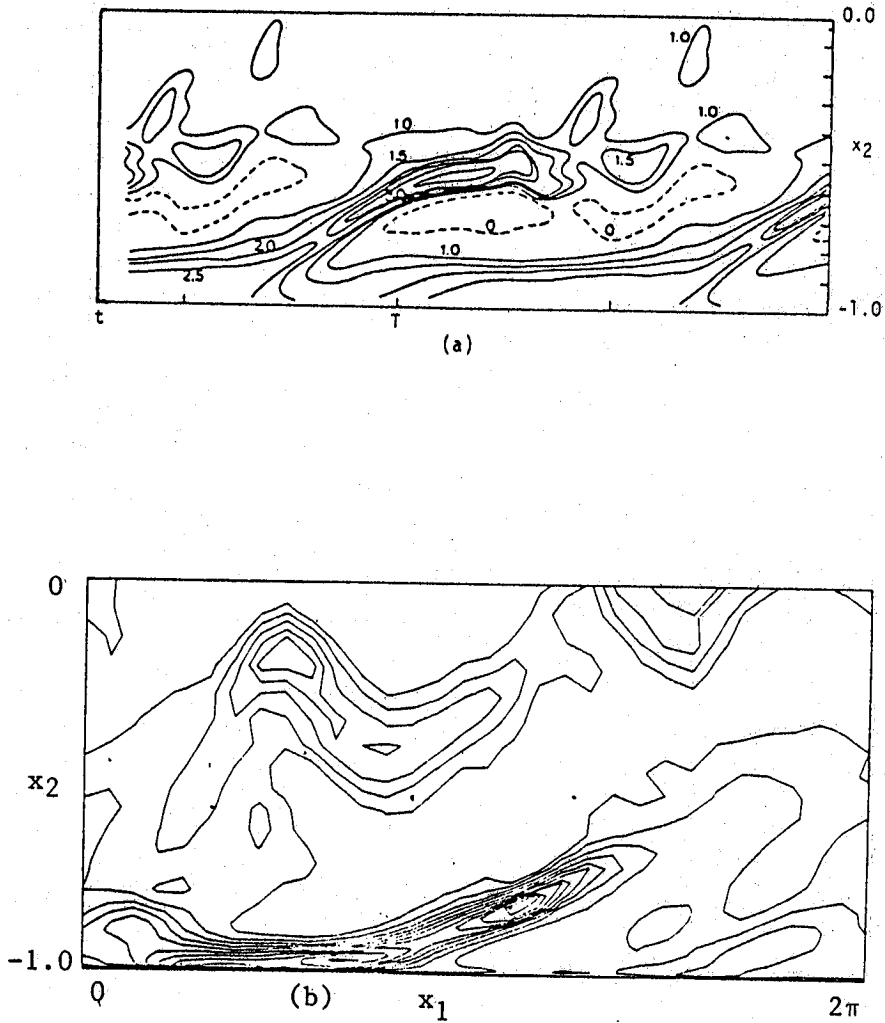
Figure 12. Contour plots of $\partial u_1/\partial x_2$. (a) Three-spike stage, figure 5 from Nishioka et al. (1981); (b) computations at $T = 27$ in the x_1-x_2 plane, contours from 0.3 to 6.8.
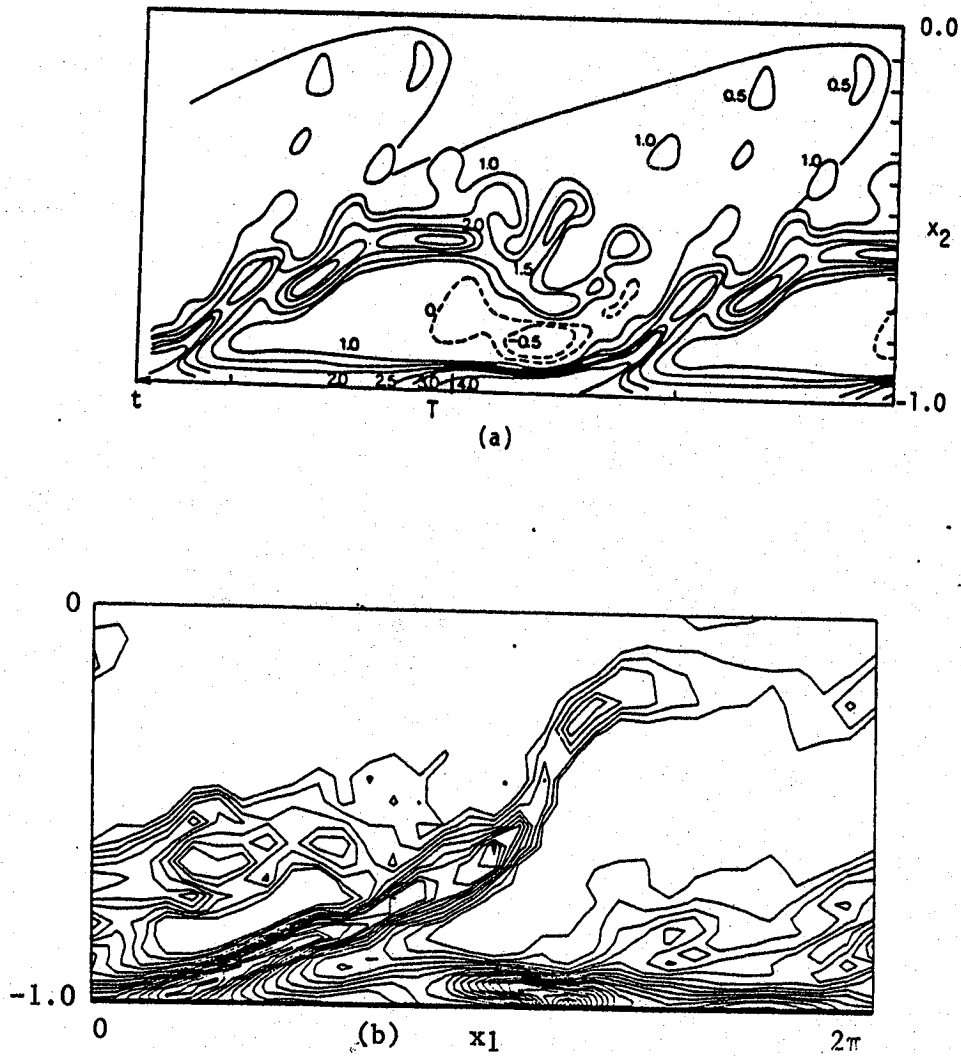
Figure 13. Contour plots of $\partial u_1 / \partial x_2$. (a) five-spike stage, figure 6 from Nishioka et al. (1981); (b) computations at $T=44$ in the x_1-x_2 plane; contours from 0.7 to 7.0. At this spanwise position, we define $x_3 \equiv (x_3)_o$.
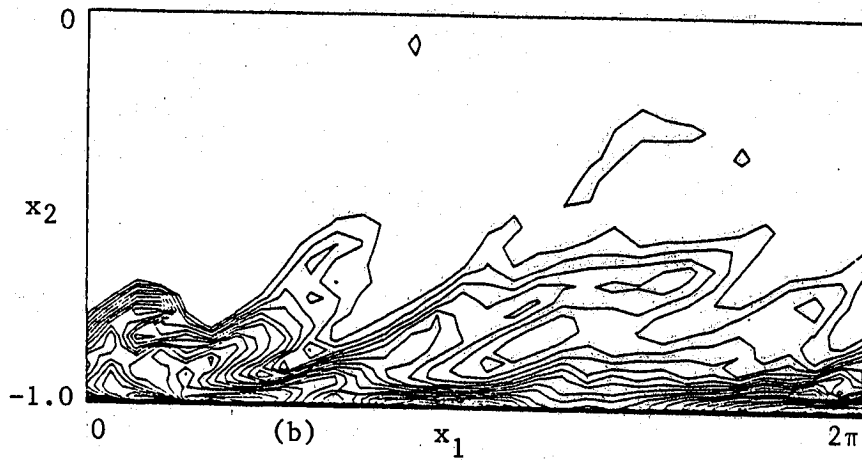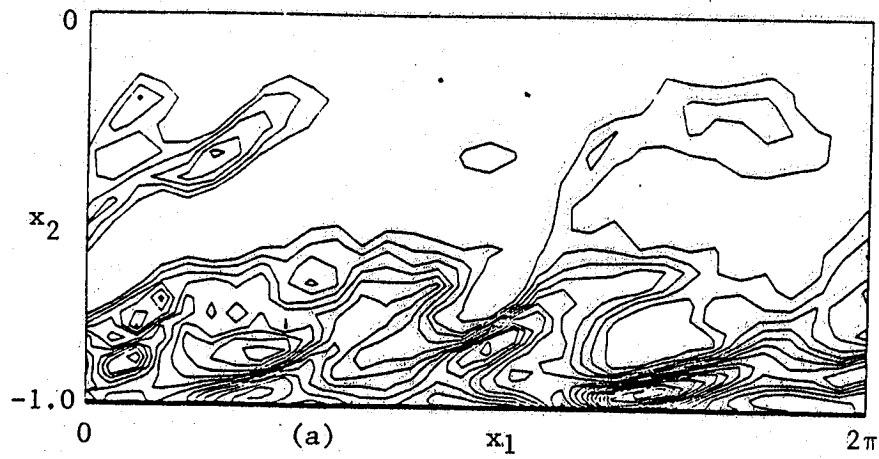
Figure 14. Contour plots of $\partial u_1/\partial x_2$ in the x_1-x_2 plane at $T = 44$; (a) $x_3 = (x_3)_0 + 2\Delta x_3$; (b) $x_3 = (x_3)_0 + 4\Delta x_3$. Here Δx_3 is the mesh size along x_3.
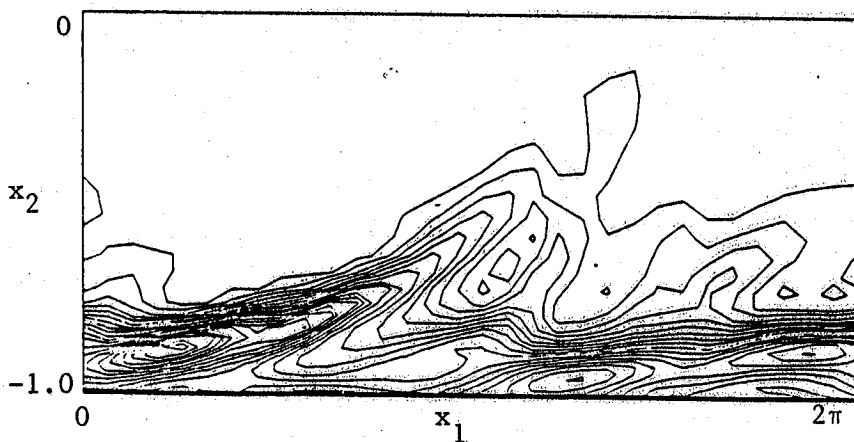
Figure 15. Contour plots of $\partial u_1/\partial x_2$ in the x_1-x_2 plane at $T = 79$; contours from 0.25 to 6.25.
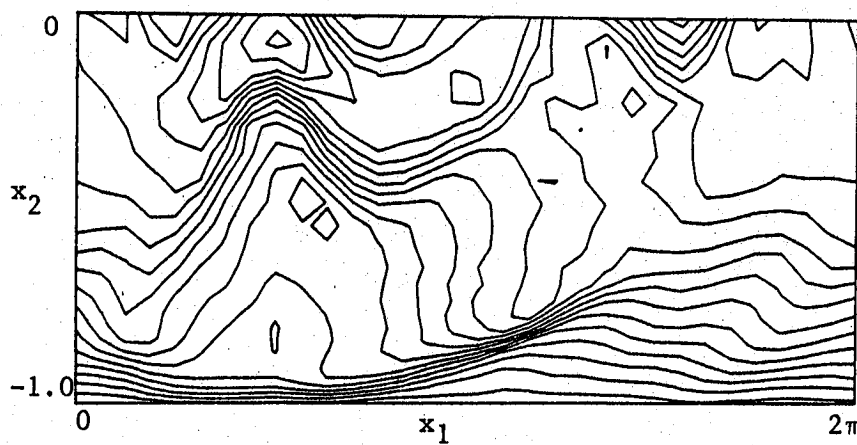
Figure 16. Contour plots of u_1 in the x_1-x_2 plane at T = 27. Contours from 0.0 to 1.08.
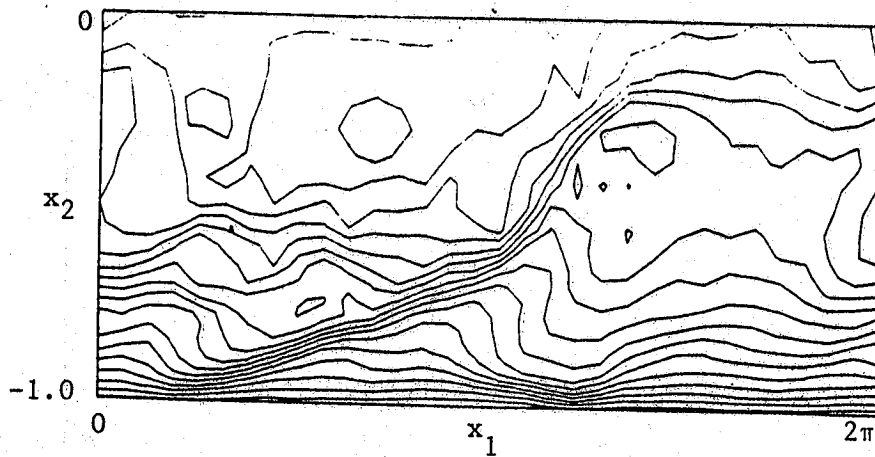
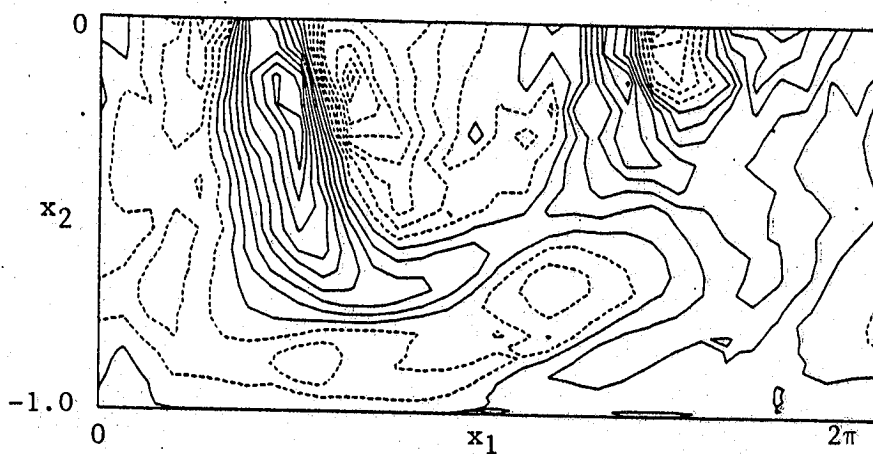Figure 17.   Contour plots of u_1 in the x_1-x_2 plane at $T = 44$.   Contours from 0.0 to 1.02.

Figure 18.   Contour plots of u_2 in the x_1-x_2 plane at $T = 27$.   Contours from -0.24 to 0.24.
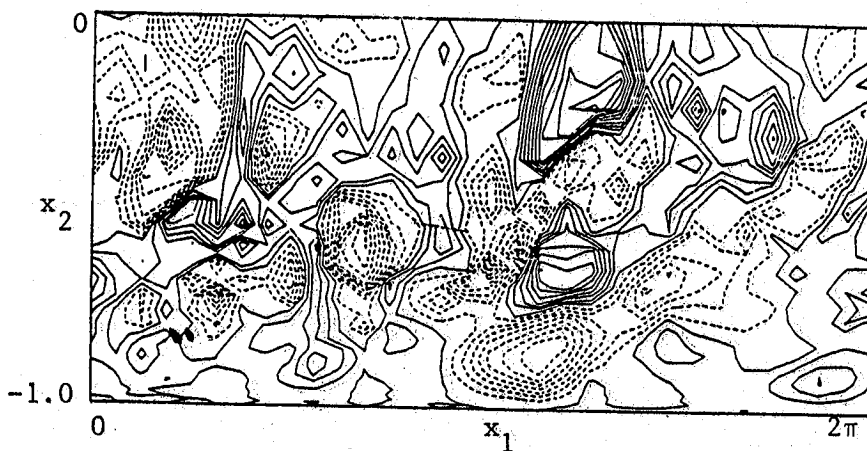

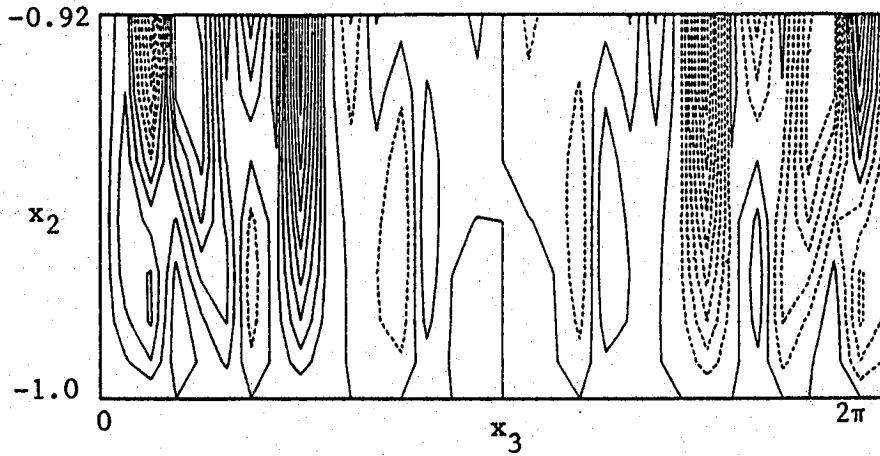Figure 19.   Contour plots of u_2 in the x_1-x_2 plane at $T = 44$.   Contours from -0.09 to 0.11.

40

Figure 20.   Contour plots of u_2 in the x_2-x_3 plane at T = 44.   Contours from
             -0.08 to 0.08.
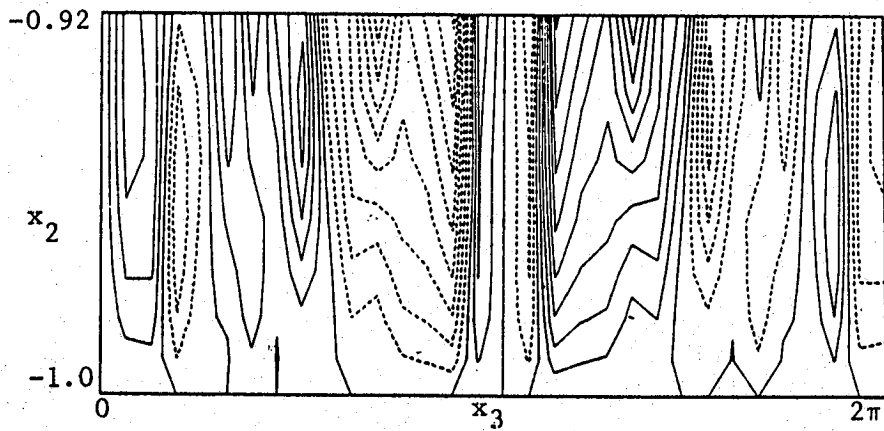

Figure 21.   Contour plots of u_2 in the x_2-x_3 plane at T = 79.   Contours from
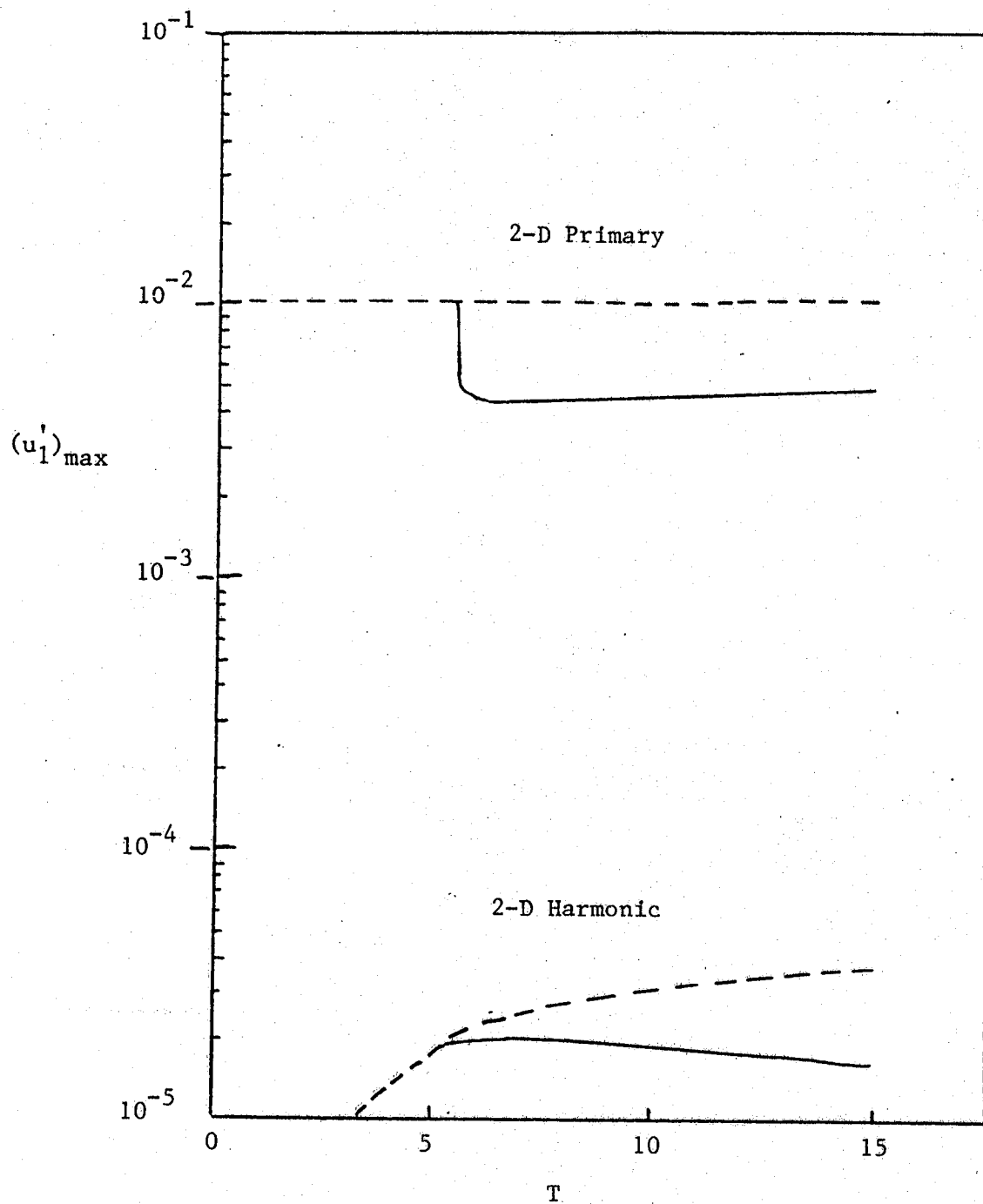   -0.06 to 0.06.
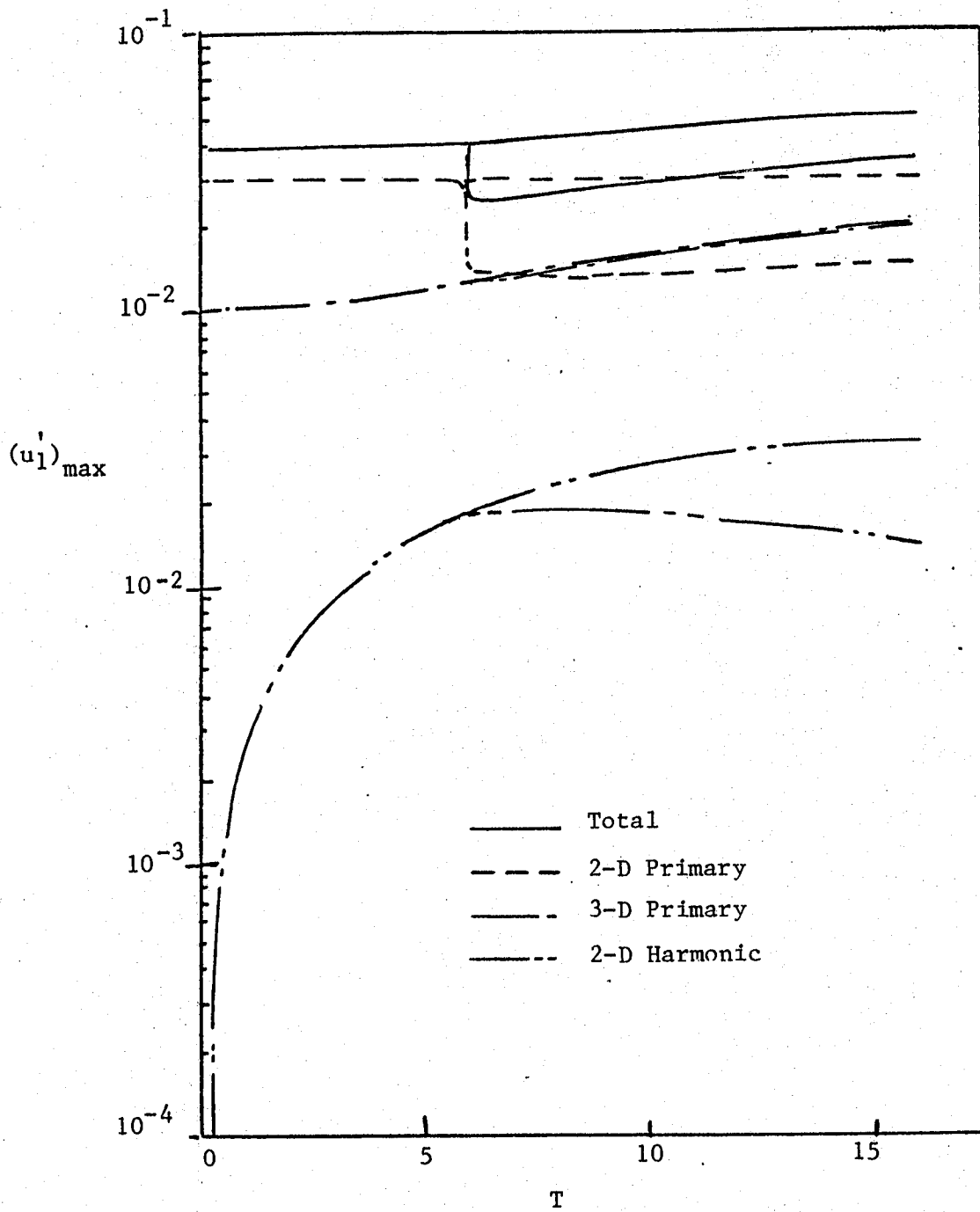
Figure 22. Two-dimensional wave cancellation.

Figure 23. Three-dimensional wave cancellation.

1. Report No. NASA CR-172298	2. Government Accession No.	3. Recipient's Catalog No.

4. Title and Subtitle	5. Report Date February 1984
Transition to Turbulence in Plane Channel Flows	6. Performing Organization Code

7. Author(s) Sedat Biringen	8. Performing Organization Report No.

9. Performing Organization Name and Address	10. Work Unit No.
Old Dominion University Mechanical Engineering & Mechanics Dept. Norfolk, VA 23508	11. Contract or Grant No. NAG1-228

12. Sponsoring Agency Name and Address	13. Type of Report and Period Covered Contractor Report
National Aeronautics and Space Administration Washington, DC 20546	14. Sponsoring Agency Code

15. Supplementary Notes

Dr. G. Goglia: O.D.U. Principal Investigator
W. D. Harvey: Langley Technical Monitor
Final Report for the period ending October 31, 1983

16. Abstract   This report describes results obtained from a numerical simulation of the final stages of transition to turbulence in plane channel flow. Three-dimensional, incompressible Navier-Stokes equations are numerically integrated to obtain the time-evolution of two- and three-dimensional finite-amplitude disturbances. Computations are performed on CYBER-203 vector processor for a 32x51x32 grid. Results are presented for no-slip boundary conditions at the solid walls as well as for periodic suction-blowing to simulate active control of transition by mass transfer. Solutions indicate that the method is capable of simulating the complex character of vorticity dynamics during the various stages of transition and final breakdown. In particular, evidence points to the formation of a Λ-shape vortex and the subsequent system of horseshoe vortices inclined to the main flow direction as the main elements of transition. Calculations involving periodic suction-blowing indicate that interference with a wave of suitable phase and amplitude reduces the disturbance growth rates.

17. Key Words (Suggested by Author(s)) Fluid Mechanics Channel Flows Transition Simulation Navier Stokes Equations	18. Distribution Statement Unclassified - Unlimited Subject Category 34

19. Security Classif. (of this report) Unclassified	20. Security Classif. (of this page) Unclassified	21. No. of Pages 46	22. Price A03

N-305